BOUNDARY CONDITIONS FOR A LATE TRIASSIC CLIMATE SIMULATION USING CESM1.2-SOM

by

JAMES ALDEN BREEN

Presented to the Faculty of the Graduate School of

The University of Texas at Arlington in Partial Fulfillment

of the Requirements

for the Degree of

MASTER OF SCIENCE IN GEOLOGY

THE UNIVERSITY OF TEXAS AT ARLINGTON

August 2022

Acknowledgments

I would like to acknowledge that a majority of the work done for this project was completed on NCAR computers, which are supported by the National Science Foundation. This research was supported by project NSF-EAR 1636629, and UTA.

A special thanks goes to the professors and faculty of the Earth and Environmental Department at UTA. In particular I would like to thank Cornelia Winguth for all of the guidance and advise she has provided. Additionally, a very special thank you goes to Mitali Gautam whose countless hours of collaboration and friendship has been an anchor for me during my graduate career. I would also like to extend my deepest gratitude to my committee members (past and present) Nathan Brown, Majie Fan, and my supervising profession Arne Winguth, whose constant support and guidance can never be understated.

On a personal note, I would like to thank my parents Rebecca Geiger and Paul Kare for their unending support and encouragement. I would also like to thank Anthony Canales who was always available to help answer my programing questions. Most of all, I would like to thank my spouse, Hunter, whose love, and support was the greatest encouragement during my time at UTA.

Abstract

BOUNDARY CONDITIONS FOR A LATE TRIASSIC CLIMATE SIMULATION USING CESM1.2-SOM

James Breen

The University of Texas at Arlington, 2022

Supervising Professor: Arne Winguth

Climate models have been widely adapted to reconstruct the environmental changes and associated mass extinction events across geologic times, such as the Younger Dryas (~12.9 Kyr), the Paleocene-Eocene Thermal Maxima (~55 Ma), and the Permian-Triassic Mass Extinction Event (~251 Ma). However, few studies have utilized climate models to investigate the potential climatic triggers of the large biological decline at the end-Triassic Mass Extinction (ETE; ~201 Ma).

In this study, global boundary conditions for the end-Triassic hothouse climate are developed in order to allow a common framework for paleoclimate simulation and to study to internal climate variability in order to better understand environmental causes of mass extinctions and to serve as an analog for future transition in warmer world.

The ETE is of particular interest because it is marked by a global negative excursion in the $\delta^{13}C_{org}$ concentration which is coincident with the onset of the observed biotic decline, potentially triggered by volcanic outgassing from the Central Atlantic Magmatic Province eruption. Such an eruption could have increased the seasonality of an already arid climate as evident in the depositional patters across the Dockum Group of western Texas. The boundary conditions developed for this study will benefit future climate modeling experiment and help gain an understand of how periodic supercritical flow deposits and monsoonal circulations were impacted by an increase in the CO_2 radiative forcing as resulting from the CAMP eruptions.

TABLE OF CONTENTS

List of Illustrations

List of Tables

Chapter 1 Introduction

Growth of the paleoclimate modeling community has resulted in demand to setup commonly used initial and boundary conditions (Herold et al., 2014) that could be utilized for model intercomparisons studies. Small variations in the initial state of a finite system that is expressed through the governing deterministic ordinary nonlinear differential equations in these climate models may lead to solutions with multiple states (Lorenz 1968; Herold et a., 2014). Given the sensitivity of climate models to their initial states, it is difficult to determine whether variations in the results between modeling groups are caused by the prescribed boundary conditions, or stem from inherent uncertainties in the model itself.

In the present study we present a set of boundary condition data for the Late Triassic in an attempt to limit the needless duplication of work and propose a series of climate sensitivity experiments to better understand environmental changes during mass extinctions triggered by a transition into a hothouse world.

1.1 The end-Triassic Background

The end-Triassic, 201.3 ± 0.2 Ma (Hillebrandt et al., 2013), culminated in one of the five most significant declines in biologic diversity of the Phanerozoic (Raup and Sepkoski, 1982; Ward et al., 2001; Dunhill et

al., 2017). The biotic decline across the Triassic-Jurassic Boundary (TJB) resulted in an 80% reduction of known living species (Ward et al., 2001). The shift in biodiversity at the TJB has been attributed to the ecological response to the intensification of the longstanding warm climate which is characteristic of the Triassic period (Rigo et al., 2020). The Triassic is unique as it is the only geologic period to be constrained by two major extinction events, the Permian-Triassic Boundary and at the aforementioned TJB. Studies of these major climatic and biotic transitions could serve as an analog for anthropogenic-induced climate change. This study focuses on the causes of the TJB climate change and seasonal climate variations associated with the larger than present ocean-land difference due to the Triassic super continent as suggested by the sedimentary record from western Gondwana. Such exceptionally strong monsoonal circulation has been first discussed for Pangaea (Kutzbach and Gallimore, 1989) and referred as megamonsoons.

1.2 Probable causes of the end-Triassic extinction

The biotic decline across the TJB has been attributed to volcanic outgassing caused by the eruption of the Central Atlantic Magmatic Province (CAMP) in central Pangea (Rigo et al., 2020). The CAMP eruption (Figure 1.2.1) occurred in four distinct pulses, with the first pulse having a

strong apparent coincidence with a decline in terrestrial and marine biodiversity (201.564 ± 0.015/0.22 Ma; Blackburn et al., 2013). There has been considerable debate as to the effects of the CAMP eruptions on the TJB extinction (Tanner et al., 2004; Onoue et al., 2016). Evidence of a major perturbation to the climate system, and stepwise biotic decline in marine organisms for ~10 Ma preceding the CAMP eruptions, suggests the end-Triassic extinction originated near the Norian-Rhaetian Boundary (NRB), ~ 208.5 Ma, (Rigo et al., 2020). A large negative global $\delta^{13}C_{org}$ excursion was coincident with a major decline in conodont, radiolarian, bivalve, and ammonite diversity during the NRB suggests outgassing from the emplacement of a large igneous province (LIP) initiated the biological decline which lasted until the TJB (Rigo et al., 2020). A bolide impact has been proposed for the cause of the CAMP eruption (Tanner et al., 2011; Onoue et al., 2016) and the extensive volcanism during the NRB (Clutson et al., 2018; Preto et al., 2020).

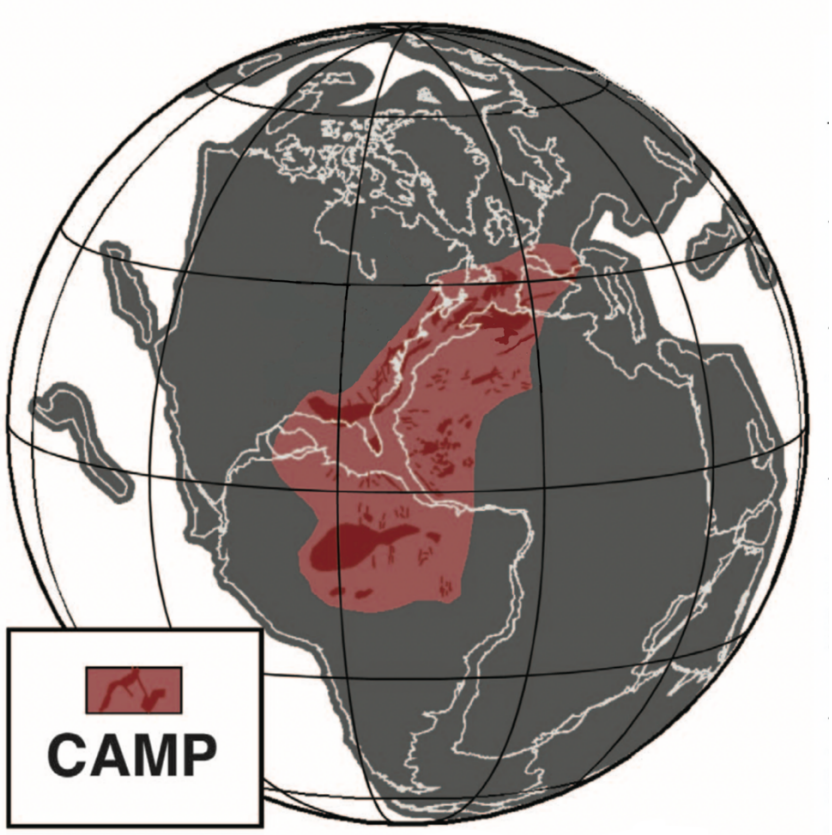

Figure 1.2.1: Extent of the CAMP flood basalts of the Late Triassic with modern day continental outlines overlaid on the Pangean continent (modified from Blackburn et al., 2013).

1.3 Late Triassic Climate

Widespread evaporite deposits spanning the equatorial to mid-latitudes of Pangea during the Triassic indicate a low meridional temperature gradient and widespread aridity (Wilson et al., 1994; Xu et al., 2012). However, abundant coal, bauxite, laterite, and kaolinite deposits across the higher latitudes of Pangea signifies humid climate belts were

less restricted towards the poles (Parrish et al., 1982; Preto et al., 2010; Xu et al., 2012).

1.4 Monsoonal Circulation

Insolation and associated heat fluxes are the main driving forces of monsoonal circulations. Differential heating of the continent and ocean during the summer results in higher temperatures, and lower atmospheric pressure over the lands surface. The warm, surface air rises while the higher-pressure air mass over the ocean transports moisture toward the low-pressure zone above the land. If the rising air mass has a sufficient concentration of water vapor, latent heat will be released into the atmosphere as condensation occurs. The release of latent heat will cause a further temperature contrast between the ocean and land, leading to an intensification of the monsoonal circulation. The winter monsoon transports moisture away from land because the pressure zones, and temperature differences are reversed. The seasonal reversal of near surface winds in areas affected by the monsoonal circulation results in a high seasonality (Wang et al., 2021).

Sedimentological evidence indicates the periodic occurrence of megamonsoons during the Late Triassic, over extratropical regions in the

modern day southwestern United States and eastern Australia (Parrish et al., 1982; Dubiel et al., 1991; Lindström et al., 2017; Walker, 2020).

Regional topography has an important effect on the development of monsoons. Coastal mountain ranges, or orographically lifted regions such as the Tibetan Plateau in southwestern China, can intensify the strength of monsoonal circulations (Fan et al., 2006; Loo et al., 2015; Revadekar et al. 2015). During summer monsoons, warm moist air will follow the steep terrane and undergo diabatic heating from sensible and latent heat fluxes. However, air masses commonly precipitate much of the moisture on the windward side of the mountain, leaving the leeward side warmer and dry, resulting in what is referred to as a rain shadow. The effect of the rain shadow is evident in the western United States, and east of the Sahyadri Mountains (otherwise known as Western Ghats Mountains) along the Deccan Plateau in India. The Southwest Indian Summer Monsoon occurs in June through September in the southwestern Indian Peninsula and is responsible for approximately 70-90% of the region's annual precipitation (Revadekar et al., 2015). Likewise, the rain shadow created by the Sahyadri Mountains largely restricts the transport of moisture leeward, resulting in arid conditions (Revadekar et al., 2015). However, humid eddies or pulses of air masses have been able to penetrate the leeward side of the Sahyadri Mountains in recent years, which has been attributed to orographic

abnormalities and possible multidecadal variations (Loo et al., 2015; Revadekar et al., 2015).

Since solar insolation has a large influence on the temperature differential required for monsoonal circulations, natural variations in Earth's orbital cycle can impact the strength of monsoons (Winguth and Winguth, 2012; Bahr et al., 2020). Three distinct orbital variations control the orientation of the Earth to the sun and are referred to as Milankovitch cycles: orbital eccentricity, obliquity, and precession of the equinoxes (Spiegel et al., 2010). The orbital path of the Earth around the Sun is not perfectly circular, instead it is slightly elliptical. A more extreme obliquity of the Earth (or tilt of Earth axis) causes cooler winter and hotter summer. The precession of the equinoxes is composed of the axial precession (or the "wobbling" motion of the Earth's rotational axis) and the precession of the elliptical path of the Earth around the Sun (also referred as the precession of the equinox). This precession of the equinox is modulated by the eccentricity, so with more extreme eccentricity and extreme precessional setting the summer insolation is increased and winter insolation reduced, particular in the subtropics, thus triggering more extreme monsoons. This study lays the foundation to explore the factors could have contributed to extreme monsoonal precipitation in the Dockum Group region, using climate sensitivity experiments.

1.5 Late Triassic Megamonsoonal Circulation and Sedimentation

The strength of the megamonsoonal circulation is thought to have intensified throughout the Triassic, reaching a maximum intensity in the Late Triassic (Parrish, 1993; Tanner et al., 2004; Preto et al., 2010). The intensification of the monsoonal circulation throughout the Triassic has been theorized to largely be a result of the northward motion of continental Pangea, with relatively symmetric land placement across the palaeoequator (Kutzbach and Gallimore, 1989; Parrish et al., 1993; Lehman and Chatterjee, 2005). The symmetric continental layout over each hemisphere, combined with the single Pangean landmass is predicted to have caused the largest possible geographically induced differential heating between the land and ocean (Kutzbach and Gallimore, 1989).

It has been proposed that the Ancestorial Rocky Mountains acted to intensify the seasonality of continental Pangea by reducing the penetration of seasonal moisture during the Late Triassic, in the same way the Sahyadri Mountain does in southwestern India (Parrish et al., 1993). The localized intensification of the monsoonal circulation along the western coast of Pangea has been theorized to increase the penetration of moisture into central Pangea during the Late Triassic (Gibson, 2018; Lamb, 2019; Walker, 2020). The fluvial systems leeward of the Ancestral Rockies has shown evidence of high discharge variability, manifesting as supercritical

flow deposits (i.e., chute and pool sedimentary structures) in the ephemeral streams spanning the Chinle Formation and Dockum Group, from modern day Nevada to western Texas, as described by Lamb, (2019) and Walker (2020). The evidence of supercritical flow conditions resulting in periodic channel scour and fill elements suggests that the climate of the Late Triassic, in the region of the Dockum Group, was dominated by monsoonal conditions (Dubiel et al., 1991; Parrish, 1993; Lehman and Chatterjee, 2005; Lamb, 2019; Walker, 2020).

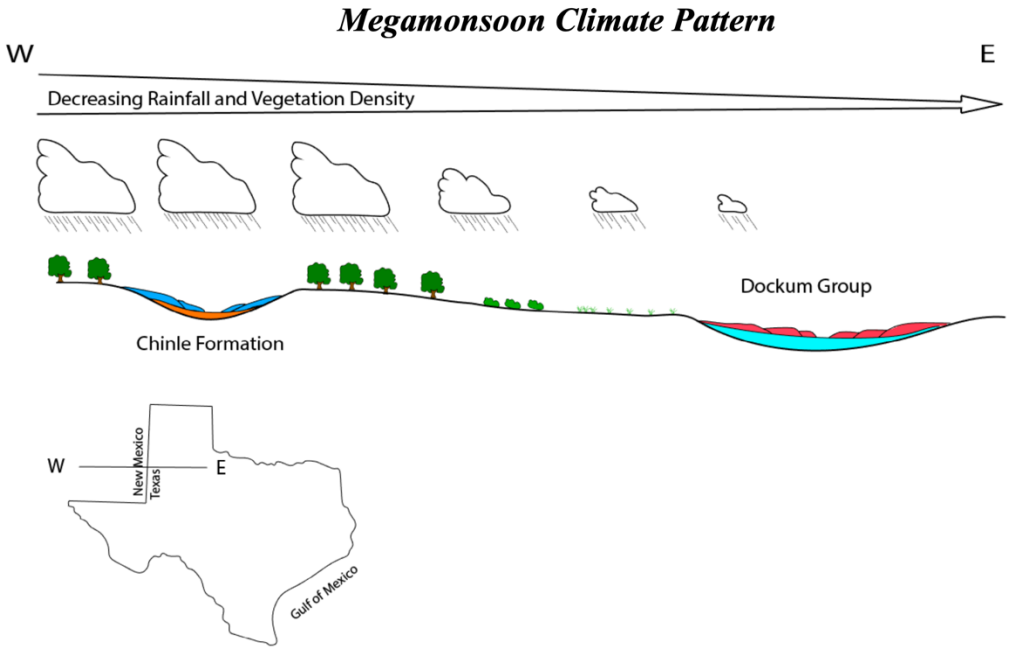

Figure 1.5.1: Simplified model showing the variation in precipitation patterns and fractional vegetation cover from the Chinle Formation (left) to the Dockum Group (right) caused by a reversal of the megamonsoonal circulation over central equatorial Pangea, resulting from volcanic outgassing in the late Norian (Image courtesy of Lamb, 2019).

Chapter 2 Objectives

In this study the framework for future climate sensitivity experiments is outlined, with focus on the Community Earth Systems Model Version 1.2. The goals of this study are to; a) provide a common set of boundary conditions for the end Triassic to be utilized by various climate models for use on different modeling frameworks and b) to use the boundary conditions to better understand internal climate variability during a hothouse climate.

Earth System Models require the creation of a wide array of input data, or boundary conditions, which are both labor-intensive and relatively slow to produce. Future studies will be able to utilize the boundary conditions provided here, thus eliminating much of the needless duplication of research which can occur between climate modeling groups. Additionally, by utilizing the same set of boundary conditions across various models, an inter-model comparison can be performed. Model intercomparison can be utilized to gain a better understanding of how model parameterization affects its overall performance and accuracy (Herold et al., 2013).

In respect to the second goal, this research could serve as an analog for future climate change as the volcanic outgassing from each pulse of the CAMP eruptions has been predicted to have released as much CO_2 as all projected anthropogenic sources for the 21st century (Capriolo et al., 2020). Although current anthropogenic CO_2 emissions are unprecedented in terms

of discharge rate, this work can be utilized by future studies to compare the climatic response of each pulse from the CAMP eruption to the modern day equivalent scenario. Additionally, the intent is to better understand the causes of monsoonal precipitation along the subtropical Pangaean west coast in the Late Triassic. This document is primarily aimed to provide background information and justification for the decisions made regarding the creation of Late Triassic boundary condition files.

This project uses climatological proxy data (such as climate sensitive sediments and depositional patterns), and model approximations, to construct the input files required to initiate a paleoclimate simulation of the Late Triassic using CESM1.2.

Chapter 3 Model Description

3.1 CESM Overview

The Community Earth Systems Model version 1.2 (CESM1.2), is a comprehensive, fully coupled climate model. CESM1.2 consists of six components: the atmosphere (Community Atmospheric Model version 4; CAM4), land (Community Land Model version 4; CLM4), ocean (the Parallel Ocean Program version 2; POP2), sea-ice (the Community Ice CodE version 4; CICE4), land-ice (the Community Ice Sheet Model; Glimmer-CISM) and river-transport (River Transport Model; RTM). These component models are connected through a central coupler (CPL7) which exchange energy and geophysical fluxes to approximate the complex interactions of the Earth's climate system more accurately. In our study with focus on hothouse climates it is not necessary to utilize Glimmer-CISM (ice sheet free conditions)

3.1.1 The Community Atmospheric Model

The Community Atmospheric Model version 4 (CAM4) is the sixth generation of atmospheric general circulation models developed by the Nation Center of Atmospheric Research. CAM4 is a three-dimensional atmospheric general circulation model which utilizes a 0.9° × 1.25° finite volume horizontal grid with 26 vertical layers, representing isobaric surfaces

between approximately 1000hPa (surface level) and 3 hPa (stratosphere) (Collins et al., 2006). CAM4 will ultimately be tightly coupled to the Community Land Model (CLM4.5) and a Slab Ocean Model (SOM), however, an initial run using the Parallel Ocean Program version 2 (POP2) must be completed to build the slab ocean model forcing files (see section 3.1.2). Further information on CAM4 can be found at: https://www.cesm.ucar.edu/models/ccsm4.0/cam/docs/description/cam4_desc.pdf.

3.1.2 The Parallel Ocean Program and Slab Ocean Model

The initialization of CESM1.2 will be completed using the Parallel Ocean Program version 2 (POP2). The POP2 component model is a level-coordinate general circulation model which approximates ocean dynamics using the three-dimensional primitive equations for a thin, stratified fluid across 60 vertical layers. The model uses for this study a nominal 1° horizontal and 60 vertical layers that non-linearly increases in thickness with depth, thus having a higher resolution near the ocean's surface and lower resolution in the deep ocean.

Given the timescale of deep-sea circulation, POP2 requires 1,500 years or more to reach a state of equilibrium. However, a state of quasi-equilibrium can be achieved in the near surface ocean waters within ~50

simulated years as seen in Winguth et al., (2010). By running POP2 to a state of quasi-equilibrium while coupled to CAM4, atmospheric processes that are less dependent on deep sea dynamics and upwelling can be reasonably approximated as seen in (Danabasoglu et al., 2009). Such an approximation can then be utilized by a Slab Ocean Model in a less computationally expensive configuration.

The Slab Ocean Model (SOM) based on the approach of Hansen et al. (1984) is a simplified one layer coupled ocean modeling component combined with a thermodynamic sea ice component originated from the CCSM3 sea ice model. The prognostic variable of SOM is the mixed layer temperature T_o while the thermodynamic sea ice model treats snow depth, surface temperature, ice thickness, ice fractional coverage, and internal energy at four layers for a single thickness category. The total heat flux of SOM is equal to the heat flux between the sea ice free ocean and the atmosphere, the heat flux from the sea ice to the atmosphere, and the heat gained when sea ice growth over the water and is governed by the following equation:

$$\rho c_p h_o \frac{\partial T_o}{\partial t} = (1 - A)F_{oa} + Q + AF_{oi} + (A - 1)F_{frz}\ , \qquad (3.1.1)$$

where ρ is the density of sea water, c_p represents the heat capacity of water, h_o is the depth of the mixed layer, T_o is the temperature of the mixed layer, F_{oa} is the net ocean-atmosphere surface heat flux, Q is the internal mixed

layer heat flux, F_{oi} is the heat exchanged with the sea ice, F_{frz} is the heat gained when ice grows over water, and A the fraction covered by sea ice.

The SOM has a variable h_o which is estimated in accordance with the method proposed by Levitus, (1982), by parametrizing the mixed layer depth as a function of salinity (Montègut et al., 2004) which satisfies the following on a 1˚ x 1˚ grid (Neale et al., 2017):

$$\sigma_t(h_o) - \sigma_t(surface) = 0.125 \ , \qquad (3.1.2.)$$

Where, $\sigma_t = (\rho_S - 1) * 10^3$, (3.1.3.)

Here, σ_t denotes a standard measure of the density of sea water and,

ρ_S is the density of sea water for a given salinity, temperature, and pressure. Equation 3.1.2 is based on the characteristics of the Subtropical Mode Water mass in the North Atlantic (Montègut et al., 2004), and defines the boundary of the mixed layer at the depth where the density of sea water is increased by 0.125 kgm^{-3} compared to the surface. A summary of constants used in the SOM can be found in Table 3.1.1.

The treatment of the mixed layer in SOM results in a relatively accurate seasonal estimation for the depth of the ocean mixed layer. Tropical regions exhibit a shallow mixed layer (~10m–30m) in the SOM, with a large seasonal variation (~10m–200m) in higher latitudes (Neale et al., 2017). To decrease the equilibration time between CAM and SOM, the

depth of the mixed ocean layer is capped at a depth of 200m (Neale et al., 2017).

This single layer model allows for a reasonable approximation of flux exchanges between the atmosphere and ocean, while substantially reducing the computational expense compared to POP2 while running the simulation (Danabasoglu and Gent, 2009). By using the Slab Ocean Model (SOM) in this study we reduced the climate integration from ~2,500 years with POP to ~50 years with SOM. Additionally, the role of deep ocean processes is assumed to have minimal impact for the depositional area of the Dockum Group in this study, but may be of interest for future investigations.

Table 3.1.1 Prescribed constants used in the Slab Ocean Model (Adapted from Neale et al., 2017).

Parameters	Constants	Value
Temperature	T_f	-1.8˚C
Ocean	ρ_o	1.026×10^3 kg m^{-3}
	C_o	3.93×10^3 J kg^{-1} K^{-1}
Ice	L_i	3.014×10^8 J M^{-3}

Since the SOM requires a fully dynamic monthly averaged ocean output to be used as a boundary condition file, POP2 will be run until a state of quasi-equilibrium is reached between the ocean and atmosphere prior to the start of the sensitivity experiments.

3.1.3 The Community Land Model

The Community Land Model version 4.5 (CLM4.5) has a complex nested grid design with three main levels to more accurately simulate land, atmosphere, soil, and plant interactions. The CLM4.5 utilizes the same horizontal resolution as CAM4 to allow less computation resources for flux exchanges between the two component models.

The first subgrid level in the CLM4.5 divides each grid point into fractional land unit types (i.e., crop, glacier, lake, urban, and vegetated land units). The land units represent regions of the largest scale spatial patterns defined by CLM4.5 and are limited to glacier, lake, and vegetated regions for paleoclimate simulations. The second subgrid level (column subgrid level) defines a vertical soil and snow cover profiles for each given land unit. The soil profile is constructed from 15 vertical layers with up to five layers reflecting potential snow cover depths. Soil moisture and energy fluxes are defined on the column subgrid level, and calculates boundary fluxes based on a weighted average of fractionally assigned plant function types (PFT) for each grid cell. The third subgrid level is defined as the PFT level which acts to define the biophysical and biogeochemical characteristics for up to 16 plant groups. The PFT level facilitates all flux transport to and from the biological regime of CLM4.5 is based on model defined characteristics of

each PFT, including bare ground. PFT are fractionally assigned to each grid cell based on a user input landcover file.

Table 3.1.2. Interpolation of Paleosols based on present day PFTs (Adopted from Goswami A., 2011 and Zobler, 1986 Soil Maps).

CESM 1.2 PFT	**Soil Types**	**Soil Color Class**
Tropical Rain Forest	Ferralsol, Nitosol, Oxisols	17
Temperate and broadleaf mixed forests	Histosol, Podsol	18
Savanna (Tropical, semi-humid)	Phaeozems	10
Broadleaf Deciduous Temperate shrub	Aridisol- Xerosol, Yermosol	6
Scelerophyllous woody plants (Warm temperate, dry summers)	Acrisol, Phaeozem, Cambizol	6
Temperate Evergreen Forests	Chernozem	18
Steppe (mid-latitude, dry summers)	Arenosol, Vertisol	10
Broadleaf Deciduous Boreal shrub	Luvisol	15
Boreal Coniferous Forest	Chernozem, Greyzem	18
Interrupted woods	Gleysol	14
Tundra	Land Ice	1
Mountains	Lithosols	20

Soil color is divided into 20 classes (Table 3.1.2) which are translated to soil albedo for visible and near infrared light in the CLM. The albedo for each color class is defined by the average monthly moisture content in the soil, and soil characteristics based on the fractional land surface cover of each grid cell. Further information on CLM4.5 can be found at: https://www.cesm.ucar.edu/models/cesm1.2/clm/models/lnd/clm/doc/UsersGuide/f101.html.

3.1.4 The River Transport Model

The River Transport Model (RTM) is designed to reroute runoff from the lands surface back to active ocean grid points in order to form a closed hydrologic cycle. The RTM has a default horizontal resolution of 0.5° x 0.5° but will be run using a 1° x 1° resolution since the atmospheric model has a comparable resolution and thus further save computational resources. The RTM routes water through each land grid cell in the direction of the steepest downhill topographic gradient. However, to prevent endorheic basins, areas with a closed basin, or closed loop in the runoff flow were redirected to allow for minimal uphill flow to the nearest ocean drainage basin. The CLM5 calculates the runoff flux which is then directed to the ocean by the RTM. Once at the ocean, the surface runoff is then passed to POP2 to facilitate near shore freshwater dispersion and salinity calculations.

3.2 Boundary Conditions for the End-Triassic

As of this study following boundary conditions have been developed:

3.2.1 Topography and Bathymetry

The paleo-topography used in the present study was provided courtesy of the PALEOMAP Project (Scotese, 2001), for the Late Norian (~210 Ma; Figure 5). The topographic data was interpolated to a 1° x 1° horizontal spatial resolution, as required by the model coupler, land model, and river runoff model. Bays and fjords were widened to a minimum of 5^{o}, and three-point costal smoothing was performed to improve model stability. Additional alterations to the bathymetry were not required, except for defining the minimum shelf depth to be 400 m to prevent insufficient energy transfer between the top waters and atmosphere. In-land topographic smoothing was not required due to the interpolation processes.

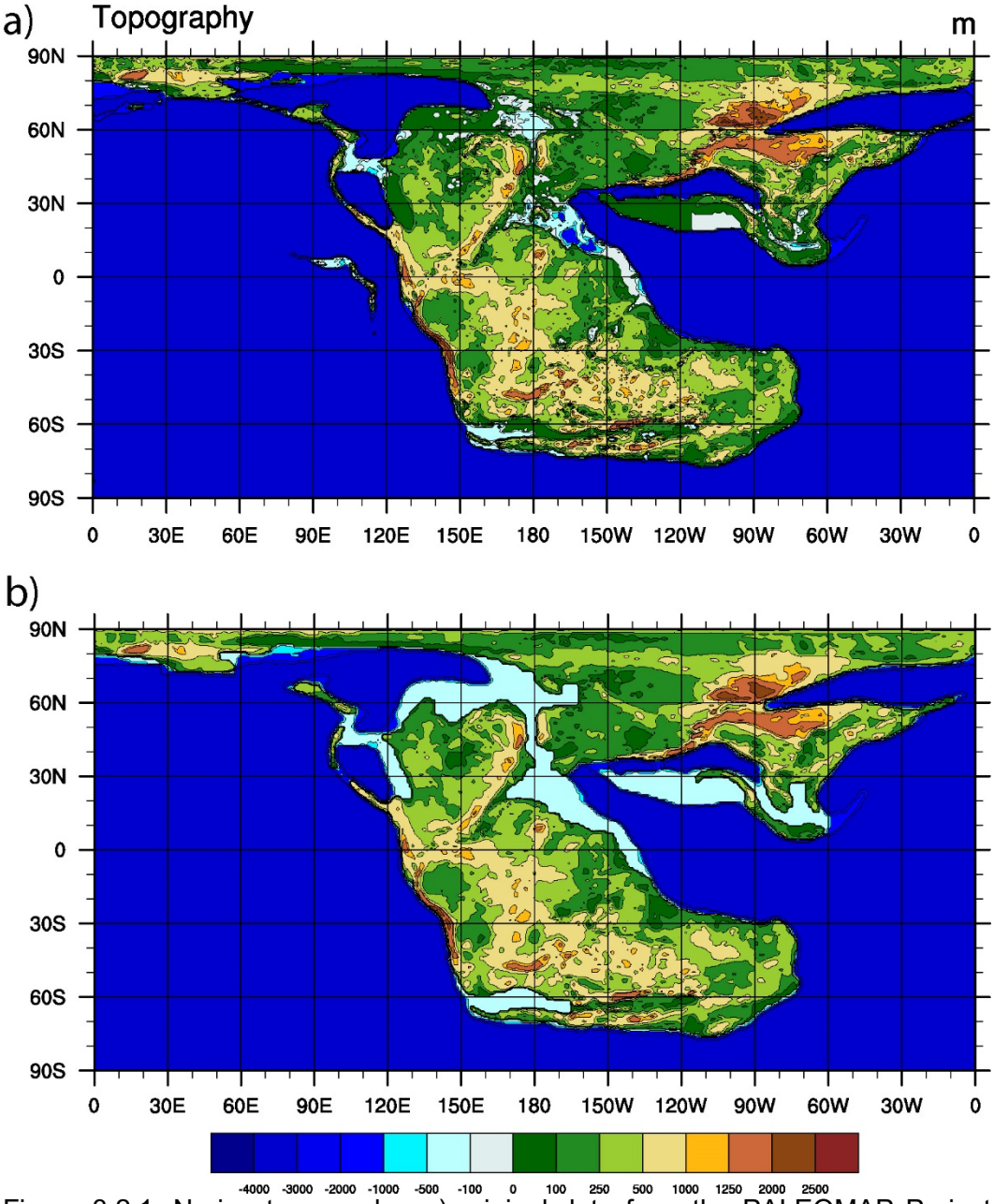

Figure 3.2.1: Norian topography; a) original data from the PALEOMAP Project (2001); b) refined paleo-topography with coastal smoothing, widening of bays and fjords, etc., used for this study.

3.2.2 Radiative forcing

To reflect the decreased solar luminosity (S) for the Late Triassic, paleoinsolation was calculated using the equation given by Caldeira and Kasting (1992):

$$S(t) = \left(1 - \frac{0.38t}{\tau_0}\right)^{-1} S_o \ , \qquad (3.2.1)$$

where t is the time from present, τ_0 is the is the approximate age of the sun, and S_0 is present day solar luminosity (1366 W m^{-2}). Solar insolation was determined to be 1342 W m^{-2} which is a reduction of 1.76% compared to modern day. The prescription of insolation is a reduction of approximately 1.76% compared to modern day.

To ensure equal solar insolation across each hemisphere, the eccentricity of Earth's orbit is representative of a circular path (eccentricity = 0), and Earth's obliquity is set to 23.5^o (Winguth et al., 2002). The current orbital parameters were additionally selected to act as a reference for future climate sensitivity experiments of the megamonsoonal circulation as described by Winguth and Winguth (2012).

Two climate sensitivity experiments using pre and post CAMP approximations of atmospheric CO_2 concentrations are planned, in addition to a control run using preindustrial atmospheric CO_2 concentrations (PAL; 280 ppmv). Estimations of atmospheric CO_2 concentrations for the pre-

CAMP eruption 4x pCO_2 PAL, or 1120 ppmv prior to the CAMP eruption (Steinthorsdottir et al., 2011; Foster et al., 2017). Post CAMP eruption pCO_2 has been approximated to have been 8x pCO_2 PAL, or 2240 ppmv.

The 4x pCO_2 PAL simulation intends to produce a baseline for the theorized megamonsoonal climate at the NRB, prior to the longstanding outgassing events that are characteristic of the end-Triassic extinction. Likewise, the 8x pCO_2 PAL simulation will be used to estimate the effect of increased CO_2 radiative forcing on the megamonsoonal climate following the CAMP eruptions, marking the end of the mass extinction event. Additional greenhouse gas prescriptions will be based on estimations for the Late Permian. A summary of the radiative forcing boundary conditions to be used in the initialization of CESM1.2 can be found in Table 3.2.1.

Table 3.2.1. Radiative forcing boundary conditions for a Late Triassic simulation (adapted from Kiehl and Shields (2005)). Note that ppmv represents concentration in parts per million by volume and S_0 is solar irradiance.

Experiment	**CO_2 (ppmv)**	**CH_4 (ppmv)**	**N_2O (ppmv)**	**S_0 (Wm^{-2})**	**Eccentricity**	**Obliquity**
Reference 1x CO_2	280	0.700	0.275	1342	23.5	0
4x CO_2	1120	0.700	0.275	1342	23.5	0
8x CO_2	2240	0.700	0.275	1342	23.5	0

3.2.3 Climate Zones and Surface Characteristics

The climate zone classification used in the present study follows that derived from Rees et. al., (2002); which has been inferred from the Köppen (1936) climate classification as a function of a regions monthly average precipitation and temperature. The Late Triassic climate zones were first prescribed based on the temperature and precipitation output of a Late Permian climate simulation, using the Community Climate System Model version 3 (CCSM3), with $12xCO_2$ radiative forcing and low cloud cover (model details are available in Gautam, 2018). The resulting climate zones where then interpolated to the Late Triassic topography (Figure 3.2.2 a). The CCSM3 data used in the first climate zone reconstruction (Figure 3.2.2 a) was selected based the topographic similarity of the Late Permian and Late Triassic, mainly a single land mass which is relatively symmetric about the equator, and evidence of widespread aridity for both times. See Table 3.2.2 for a summary of the climate zone prescription requirements with associated land cover with the equivalent modern plant types.

Refinement of the Late Triassic climate zones was completed using lithological proxy data from Xu et al., (2012), specifically for the region which is now western Texas and the high latitudes (Figure 3.2.2 b). Additional adjustments to the climate zones were made for the remaining regions to

reflect the reconstruction made using the HadAM3 general atmospheric circulation model presented in Sellwood and Valdes (2006) (Figure 3.2.2 c).

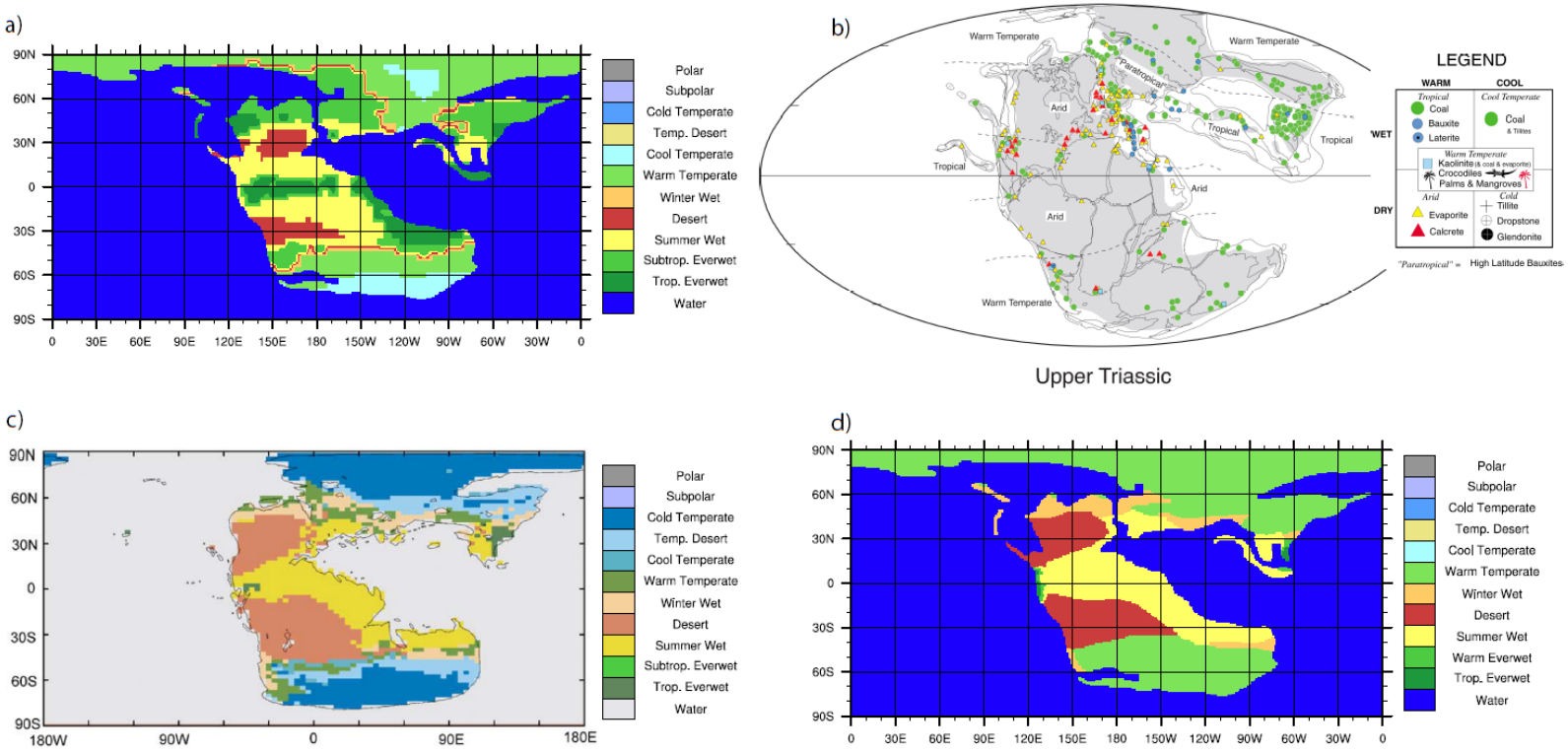

Figure 3.2.2: Climate zone reconstruction of the Late Norian; a) Climate zones reconstructed from temperature and precipitation outputs from a CCSM3 12x CO_2 simulation of the Permian-Triassic boundary, which was interpolated to the Norian topography; b) Climate proxy data courtesy of Xu et al., (2012) that was used to refined prescribed climate zones; c) Climate zone reconstruction from HadAM3 model output courtesy of Sellwood and Valdes, (2006); d) Final climate zone reconstruction used in the creation of Late Triassic boundary condition files.

Table 3.2.2: Summary of LSM land cover type and PFT's prescribed to each climate zone.

No.	Climate Zones	Modern Vegetation	LSM Landcover Types CESM 1.2	Plant Functional Types (PFTs)
1	Polar	Tundra	Tundra	broadleaf deciduous boreal shrub or bare
2	Sub-polar	Boreal Forest	Deciduous Forest Tundra (Interrupted woods)	Needleleaf Evergreen Boreal Tree
3	Cold Temperate, arid	Boreal Coniferous Forest	Cool Needleleaf Deciduous Tree	Needleleaf deciduous boreal tree
4	Temperate Desert, dry summers	Desert	Semi-desert	broadleaf deciduous temperate shrub
5	Cool Temperate	Steppe or Nemoral broadleaf Deciduous Forest	Cool Deciduous Broadleaf Forest	broadleaf deciduous boreal tree
6	Warm Temperate	Temperate Evergreen Forest	Warm Broadleaf Deciduous Tree	broadleaf deciduous temperate tree
7	Winter-wet	Sclerophyllous woody plants	Cool Mixed Forest	needleleaf evergreen boreal tree, broadleaf deciduous boreal tree
8	Desert	Desert	Desert	Desert (bare)
9	Summer-wet	Savanna	Savanna	broadleaf deciduous tropical tree
10	Subtropical Ever-wet	Temperate bro adleaf and mixed forests	Warm Mixed Forest	needleleaf evergreen temperate tree, broadleaf deciduous temperate tree
11	Tropical Ever-wet	Tropical Rain Forest	Tropical	broadleaf evergreen tropical tree
12	Water*	-	Ocean*	-

The climate zone classifications serve as an analog for the creation of plant functional types (PFT; Table 3.2.3; depending on paleo-soil albedo, soil texture, and fractional vegetation cover files as described in CLM4.5; Olsen et al., 2013) since plant type geographic distribution depends on both seasonal temperature and precipitation The fractional land cover type, soil texture, and soil color (Table 3.2.4) were prescribed by utilizing a tool provided by the University Corporation for Atmospheric Research, which assigns modern day physio-chemical and anatomical characteristics of the dominant plant functional types found to a corresponding climate zone.

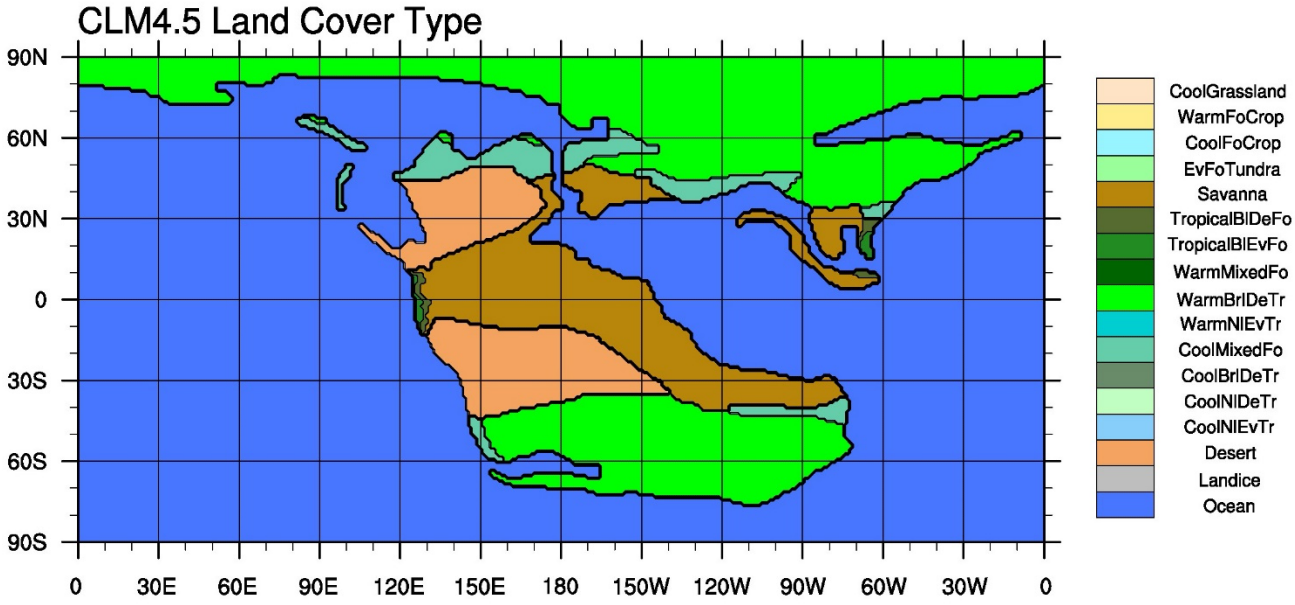

Figure 3.2.3: Prescribed Late Norian land cover types. Bl = Broadleaf, De = Deciduous, Ev = Evergreen, Fo = Forest, and Tr = Tree.

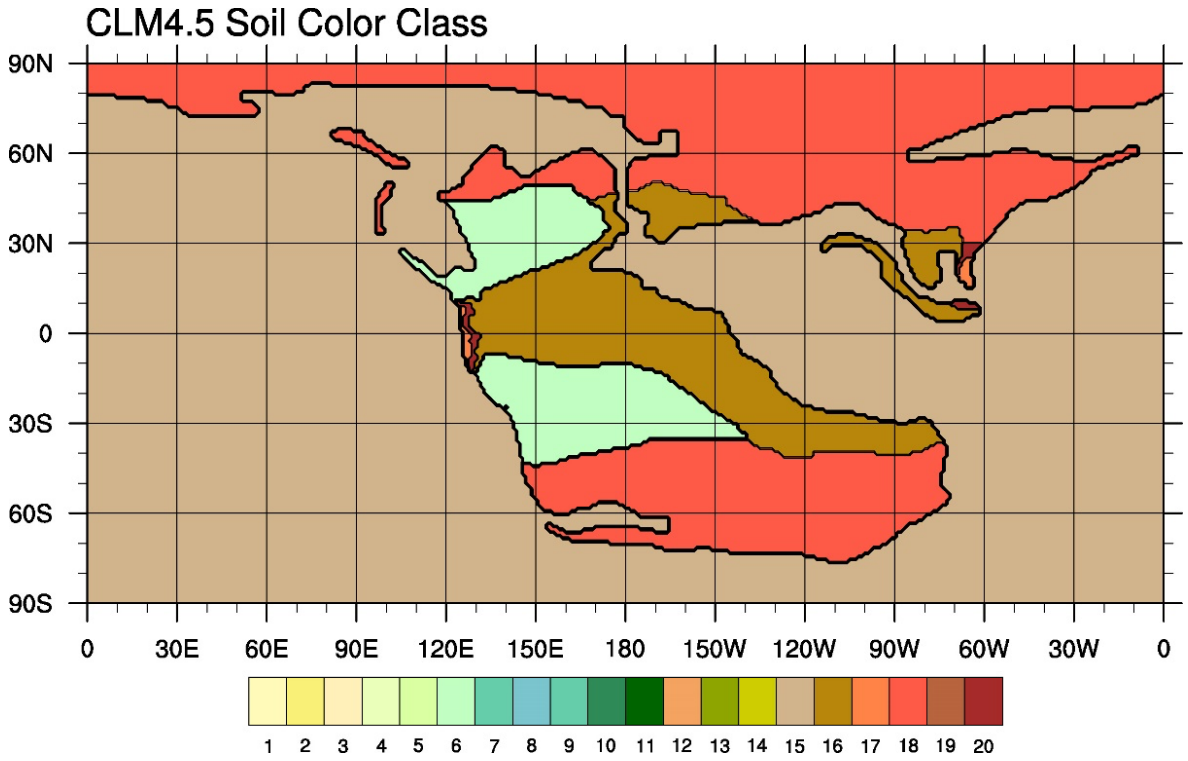

Figure 3.2.4: Late Norian soil color class prescriptions, based on modern day PFT and soil characteristics.

3.2.4 Aerosols

Five chemical species of aerosols are modeled in CAM4 including sea salt, soil dust, black-organic carbon, sulfate, and volcanic sulfuric acid. The aerosol chemical species are further divided into 10 subgroups which have three optical properties: 1) specific extinction, 2) single scattering albedo, and 3) asymmetry parameter.

CAM4 allows for two different treatments of aerosols; the bulk aerosol model method, and the prescribed aerosol method. The BAM method requires the prescription of key particle classes which are used to calculate aerosol forcings. Following the

completion of the CAM4-BAM configuration, the resultant aerosol fluxes are used to construct monthly aerosol forcings for use in the prescribed aerosol method as described in Heavens et al., (2012).

In this study, three gas species (dimethyl sulfate; DMS, SO_2, and SO_4) and two particle classes (organic carbon; OC1, and black carbon; BC1) that are important in aerosol formation, form the boundary conditions for the CM4-BAM model configuration. All aerosol precursors are prescribed to a 0.9˚ X 1.25˚ grid by zonally averaging pre-industrial forcings and interpolating the results to fit the topographic distribution of the Late Triassic (Figure 3.2.5 a-e).

The zonal distribution of DMS prescribed in this study required extra consideration to the source location. DMS is mainly emitted over the ocean and is a result of DMS-producing plankton-types like Phaeocystis, however, small concentrations of DMS are emitted over ice-free land (Heavens et al., 2012). To account for this difference, a zonal average of pre-industrial DMS was calculated over the land and ocean which were interpolated to Late Triassic topography (Figure 3.2.5 c). Other sulfide gas species (i.e., SO_2 and SO_4) handled in the BAM are assumed to only be the result of volcanic outgassing which is of importance for the Late Triassic given the largescale volcanism of the CAMP eruptions. Uncertainties in spatiotemporal distribution of the volcanic outgassing during the CAMP eruption, the SO_2 and SO_4 distribution presented here (Figure 3.2.5 d-e) is not meant to represent the conditions for the Late Triassic. Instead,

a single volcanic plumb with a concentration equal to the maximum pre-industrial concentrations was placed near the center of the main pulses for the CAMP eruption.

Additionally, work has been started to construct a set of prescribed aerosol forcings out of a late Permian CAM4-BAM simulation to serve as boundary condition for the Late Triassic. The use of Permian aerosol forcings to construct the Late Triassic aerosol boundary conditions is required because the BAM requires sea surface temperature data prior to initialization. Since there is not such data available for the Late Triassic, and given the number of similarities to the late Permian, both in terms of continental configuration, climate, and volcanic activity, we assume the PTB BAM forcings will be a reasonable approximation for the TRJ, with exception to placement and distribution of the respective volcanic plumbs.

While current estimates of total volcanic CO_2 outgassing during the eruption of the Siberian Traps (end Perriman) and the CAMP flood basalt are 100,000 Gt CO_2 (Svensen et al., 2009; Capriolo et al., 2020), the geographic distribution of the eruptions pose an issue. The pulses of the CAMP eruption have a greater geographic distribution compared to that of the Siberian Traps resulting in the rescaling of the end Permian volcanic aerosols as to better fit the Late Triassic.

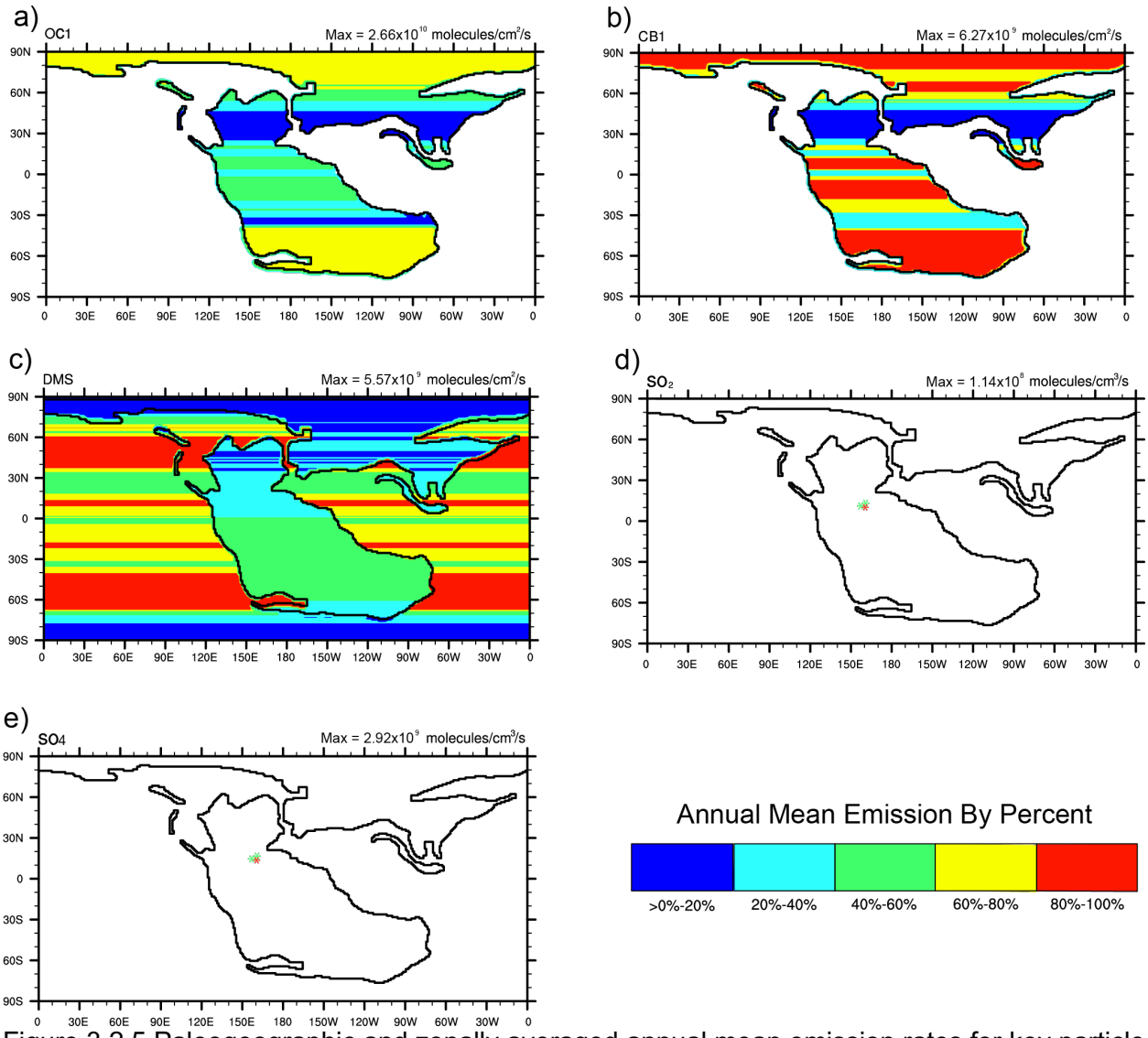

Figure 3.2.5 Paleogeographic and zonally averaged annual mean emission rates for key particle classes (a-b) and gas species (c-e) involved in aerosol formation. Figure adapted from Heavens et al., (2012).

Chapter 4 Concluding Summary and Future Outlook

This project has described a comprehensive set of boundary conditions for a Late Triassic climate simulation which include topography, radiative forcings, vegetation cover, soil color, and aerosol fluxes. The resolution of the atmospheric boundary conditions are two times greater than the default, which allows for increased model accuracy, especially in mesoscale circulation. In addition to greater accuracy, the atmospheric resolution is course enough to not require vast computational resources, unlike grids on the scale of 1 km – 10 km. Likewise, if coupled to a SOM, these boundary conditions can be utilized on a small university computer cluster, or potential on higher end desktop computers.

It should be noted that many of the boundary conditions provided here (i.e., topography, river runoff, vegetation, soil color, and insolation) were derived from model approximations. Due to the lack of reliable proxy data, modern day analogs were required to construct the LSM boundary conditions. Likewise, given there were no readily available dataset for the distribution of Late Triassic aerosols, two sets of boundary conditions were created for use in different model configurations.

The lack of paleo-topography, land surface, and radiative forcing proxy data for the deep-time climates has added to the uncertainties in past climate predictions. There is a great need to further the efforts placed on

model validation studies through the use of paleoclimate proxy data, and model intercomparisons.

References

Bahr, A., G. Kolber, S. Kaboth-Bahr, L. Reinhardt, O. Friedrich, and J. Pross, 2020: Mega-monsoon variability during the late Triassic: Re-assessing the role of orbital forcing in the deposition of playa sediments in the Germanic Basin. *J. Sedimentology*, **67**, 951-970, https://doi.org/10.1111/sed.12668.

Blackburn, T. J., P. E. Olsen, S. A. Bowring, N. M. McLean, D. V. Kent, J. Puffer, G. McHome, E. T. Rasbury, and M. Et-Touhami, 2013: Zircon U-Pb geochronology links the end-Triassic extinction with the Central Atlantic Magmatic Province. *J. Science*, **340**, 941-945, https://doi.org/10.1126/science.1234204.

Caldeira, K., and F. J. Kasting, 1992: The life span of the biosphere revisited. *J. Nature*, **360**, 721-723, https://doi.org/10.1038/360721a0.

Capriolo, M., A. Marzoli, L. E. Aradi, S. Callegaro, J. D. Corso, R. J. Newton, B. J. W. Mills, P. B. Wignall, O. Bartoli, D. R. Baker, N. Youbi, L. Remusat, R. Spiess, and C. Szadò, 2020: Deep CO_2 in the end-Triassic Central Atlantic Magmatic Province. *Nature Communications*, **11**, https://doi.org/10.1038/s41467-020-15325-6.

Clutson, M. J., D. E. Brown, and L. H. Tanner, 2018: Distal Processes and effects of multiple Late Triassic terrestrial bolide impacts: Insights from the Norian Manicouagan Even, northeastern Quebec, Canada. *Topics in Geology*, **46**, 127-187, https://doi.org/10.1007/978-3-319-68009-5_5.

Cornet, B., 1993: Applications and limitations of palynology in age, climatic, and paleoenvironmental analyses of Triassic sequences in North America. *New Mexico Museum of Natural History and Science Bulletin*, **3**, 75-93.

Danabasoglu, G., and P. R. Gent, 2009: Is it accurate to use a slab ocean model?. *J. Climate*, **22**, 2494-2499, https://doi.org/10.1175/2008JCLI2596.1.

Dickinson, W. R., G. E. Gehrels, and R. J. Stern, 2010: Late Triassic Texas uplift preceding Jurassic opening of the Gulf of Mexico: Evidence from U-Pb ages of detrital zircons. *Geosphere*, **6**, 641-662, https://doi.org/10.1130/GES00532.1.

Dunay, R. E., and M. J. Fisher, 1979: Palynology of the Dockum Group (upper Triassic), Texas, U.S.A.. *Palaeobotany and Palynology*, **28**, 61-92, https://doi.org/10.1016/0034-6667(79)90025-3.

Dunhill, A. M., W. J. Foster, J. Sciberras, and R. J. Twitchett, 2017: Impact of the Late Triassic mass extinction on functional diversity and composition of marine ecosystems. *J. Palaeontology*, **61**, 133-148, https://doi.org/10.1111/pala.12332.

Dubiel, R. F., J. T. Parrish, J. M. Parrish, S. C. and Good, 1991: The Pangaean megamonsoon evidence from the Upper Triassic Chinle Formation, Colorado Plateau. *PALAIOS*, **6**, 347-370, https://doi.org/10.2307/3514963.

Fan, M., C. Song, D. L. Dettman, X. Fang, and X. Xu, 2006: Intensification of the Asian winter monsoon after 7.4 Ma: Grain-size evidence from the Linxia

Basin, northeastern Tibetan Plateau, 13.1 Ma to 4.3 Ma. *Earth and Planetary Science Letters*, **248**, 186-197, https://doi.org/10.1016/j.epsl.2006.05.025.

Foster, G. L., D. L. Royer, and D. J. Lunt, 2017: Future climate forcing potentially without precedent in the last 420 million years. *Nature Communications*, **8**, https://doi.org/10.1038/ncomms14845.

Fielding C. R., J. P. Allen, J. Alexander, and M. R. Gibling, 2009: Facies model for fluvial systems in the seasonal tropics and subtropics. *J. Geology*, **37**, 623-626, https://doi.org/10.1130/G25727A.1.

Gautam, M. D., 2018: Simulation of climate across the Permian-Triassic Boundary with a focus on phytogeographical data analysis. Master's thesis, The University of Texas at Arlington.

Gibson, S. Z., 2018: A new species of Lasalichthys (Actinopterygii, Redfieldiiformes) from the Upper Triassic Dockum Group of Howard County, Texas, with revisions to the genera Lasalichthys and Synorichthys. *J. Vertebrate Paleontology*, https://doi.org/10.1080/02724634.2018.1513009.

Goswami, A., 2011: Predicting the geographic distribution of ancient soils with special reference to the Cretaceous. Ph.D. Thesis. University of Texas at Arlington.

Hansen, J., A. Lacis, D. Rind, G. Russell, P. Stone, I. Fung, R. Ruedy, and J. Lerner, 1984: Analysis of feedback mechanisms, in climate processes and climate sensitivity, *American Geophysics*, **29**, https://doi.org/10.1029/GM029p0130.

Heavens, N.G., C. A. Shields, and N. M. Mahowald, 2014: A paleogeographic approach to aerosol prescription in simulations of deep time climate. *J. Advances in Modeling Earth Systems*, **4**, https://doi.org/10.1029/2012MS000166.

Hillebrandt, A. V., L. Krystyn, W. M. Kürschner, N. R. Bonis, M. Ruhl, S. Richoz, M. A. N. Schobben, M. Urlichs, P. R. Brown, K. Kment, C. A. McRoberts, M. Simms, and A. Tomãsových, 2013: The global stereotype sections and point (GSSP) for the base if the Jurassic system at kuhjock (Karwendel Mountains, Northern Calcareous Alps, Tyrol, Austria). *Episodes*, **36**, 162-198, https://doi.org/10.18814/epiiugs/2013/v36i3/001.

Herold, N., J. Buzan, M. Seton, A. Goldner, J. A. M. Green, R. D. Müller, P. Markwick, and M. Huber, 2014: A suite of early Eocene (~55 Ma) climate model boundary conditions. *Geoscience Model Development*, **7**, 2077-2090, https://doi.org/10.5194/gmd-7-2077-2014.

Kiehl, J. T., and Shields, C. A., 2005: Climate simulation of the latest Permian: Implications for mass extinction. *J. Geology*, **33**, 757-760. https://doi.org/10.1130/G21654.1.

Kutzbach, J. E., and R. G. Gallimore, 1989: Pangean climates: megamonsoons of the megacontinent, *J. Geophysical Research*, **94**, 3341-3357, https://doi.org/10.1029/JD094iD03p03341.

Lamb, G. H., 2019: An architectural analysis and depositional interpretation of the Dockum Group in the west Texas high plains. Master's thesis, Texas Christian University.

Lehman, T., and S. Chatterjee, 2005: Depositional setting and vertebrate biostratigraphy of the Triassic Dockum Group of Texas. *J. Earth System Science*, **114**, 325-351, https://doi.org/10.1007/BF02702953.

Lindström, S., B. V. Schootbrugge, K. H. Hansen, G. K. Pedersen, P. Alsen, N. Thibault, K. Dybkjaer, C. J. Bjerrum, and L. H. Nielsen, 2017: A new correlation of Triassic-Jurassic boundary successions in NW Europe, Nevada and Peru, and the Central Atlantic Magmatic Province. *Palaeogeography, Palaeoclimatology, Palaeoecology*, **470**, 80-102, https://dx.doi.org/10.1016/j.palaeo.2016.12.025.

Loo, Y. Y., L. Billa, and A. Singh, 2015: Effect of climate change on seasonal monsoon in Asia and its impact on the variability of monsoon rainfall in Southeast Asia. *Geoscience Frontiers*, **6**, 817-823, https://doi.org/10.1016/j.gsf.2014.02.009.

Montègut, C.B., G. Madec, A. S. Fischer, A. Lazar, and D. Ludicone, 2004: Mixed layer depth over the global ocean: an examination of profile data and a

profile-based climatology, *J. Geophysics Research*, **109**, https://doi.org/10.1029/2004JC002378.

Neale, R. B., C. A. Gettelman, P. H. Park, and D. L. Williamson, 2017: CAM5 scientific guide, Chapter 7, University Corporation for Atmospheric Research, https://ncar.github.io/CAM/doc/build/html/cam5_scientific_guide/slab_ocean.html.

Oleson, K., D. M. Lawrence, G. B. Bonan, B. Drewniak, M. Huang, C. D.Koven, Z. Yang, 2013: Technical description of version 4.5 of the Community Land Model (CLM)(No.NCAR/TN-503+STR). https//doi.org/10.5065/D6RR1W7M.

Onoue, T., H. Sato, D. Yamashita, M. Ikehara, K. Yasukawa, K. Fujinaga, Y. Kato, and A. Matsuoka, 2016: Bolide impact triggered the Late Triassic extinction event in equatorial Panthalassa. *Science Reports*, **6**, https://doi.org/10.1038/srep29609.

Parrish, J. T., A. M. Ziegler and C. R. Scotese, 1982: Rainfall and the distribution of coals and evaporites in the Mesozoic and Cenozoic. *Palaeogeography, Palaeoclimatology, Palaeoecology*, **40**, 67-101, https://doi.org/10.1016/0031-0182(82)90085-2.

Parrish, J. T., 1993: Climate of the Supercontinent Pangea. *J. Geology*, **101**, 215-233, https://doi.org/10.1086/648217.

Preto, N., E. Kustatscher, and P. B. Wignall, 2010: Triassic climates – State of the art and perspectives. *Palaeogeography, Palaeoclimatology, Palaeoecology*, **290**, 1- 10, https://doi.org/10.1016/j.palaeo.2010.03.015.

Raup, D. M., and J. J. Sepkoski, 1982: Mass Extinctions in the Marine Fossil Record. *J. Science*, **215**, 1501-1503, https://doi.org/10.1126/science.215.4539.1501.

Rees, P. M., A. M. Ziegler, M. T. Gibbs, J. E. Kutzbach, P. J. Behling, and D. B. Rowley, 2002: Permian phytogeographic patterns and climate data/model comparisons. *J. Geology*, **110**, 1-31, https://doi.org/10.1086/324203.

Revadekar, J. V., H. Varikoden, and V. V. Sapre, 2015: Variability in Summer Monsoon Rainfall over Pune, a Leeward Side Station of Western Ghats in India. *Bulletin of Indian Meteorological Society*, **41**, 11-19.

Rigo, M., T. Onoue, L. H. Tanner, S. G. Lucas, L. Godfrey, M. E. Katz, M. Zaffani, K. Grice, J. Cesar, D. Yamashita, M. Maron, L. S. Tackett, H. Campbell, F. Tateo, G. Concheri, C. Agnini, M. Chiari, and A. Bertinelli, 2020: The Late Triassic Extinction at the Norian/Rhaetian boundary: Biotic evidence and geochemical signature. *Earth and Science Reviews*, **204**, https://doi.org/10.1016/j.earscirev.2020.103180.

Sato, H., Y. Takaya, K. Yasukawa, K. Fujinaga, T. Onoue, and Y. Kato, 2020: Biotic and environmental changes in the Panthalassa Ocean across the

Norian (Late Triassic) impact event. *Progress in Earth and Planetary Science*, **7**, 61, https://doi.org/10.1186/s40645-020-00371-x.

Sellwood, B. W., and Valdes, P. J., 2006: Mesozoic climates: General circulation models and the rock record. *Sedimentary Geology*, **190**, 269-287, https://doi.org/10.1016/j.sedgeo.2006.05.013.

Scotese, C. R., 2001. Atlas of Earth History, Volume 1, Paleogeography, PALEOMAP Project, Arlington, Texas.

Spiegel, D. S., S. N. Raymond, C. D. Dressing, C. A. Scharf, and J. L. Mitchell, 2010: Generalized Milankovitch cycles and long-term climatic habitability. *Astrophysical J.*, **721**, 1308-1318, https://doi.org/10.1088/0004-637X/721/2/1308.

Steinthorsdottir, M., A. J. Jeram, and J. C. McElwain, 2011: Extremely elevated CO_2 concentrations at the Triassic/Jurassic boundary. *Palaeogeography, Palaeoclimatology, Palaeoecology*, **308**, 418-432, https://doi.org/10.1016/j.palaeo.2011.05.050.

Tanner, L. H., S. G. Lucas, and M. G. Chapman, 2004: Assessing the record and causes of Late Triassic extinction. *Earth and Science Reviews*, **65**, 103-139, https://doi.org/10.1016/S0012-8252(03)00082-5.

Tanner, L. H., J. F. Hubert, B. P. Coffey, and D. P. McInerney, 2011: Stability of atmospheric CO_2 levels across the Triassic/Jurassic boundary. *J. Nature*, **411**, 675-677, https://doi.org/10.1038/35079548.

Walker, S. P., 2020: Profiles and paleohydrology of supercritical rivers, the Triassic Dockum Group of West Texas. Master thesis, Texas Christian University.

Wang, B., M. Biasutti, M. Byrne, C. Castro, C. Chang, K. Cook, F. Fu, A. Grimm, K. Ha, H. Hendon, A. Kitoh, R. Krishnan, J. Lee, J. Li, J. Liu, A. Moise, S. Pascale, M. Roxy, A. Seth, C. Sui, A. Turner, S. Yang, K. Yun, L. Zhang, and T. Zhou, 2021: Monsoons Climate Change Assessment. *American Meteoritical Society*, https://doi.org/10.1175/BAMS-D-19-0335.1.

Ward, P. D., J. W. Haggart, E. S. Carter, D. Wilbur, H. W. Tipper, and T. Evans, 2001: Sudden Productivity Collapse Associated with the Triassic-Jurassic Boundary Mass Extinction. *J. Science*, **292**, 1148-1151, https://doi.org/10.1126/science.1058574.

Wilson, K. M., D. Pollard, W. W. Hay, S. L. Thompson, and C. N. Wold, 1994: General circulation model simulations of Triassic Climates: Preliminary results. *GSA Special Paper*, **288**, 91-116, https://doi.org/10.1130/SPE288-p91.

Winguth, A. M. E., C. Heinze, J. E. Kutzbach, E. Maier-Reimer, U. Mikolajewicz, D. Rowley, A. Rees, and A. M. Ziegler, 2002: Simulated warm polar currents during the middle Permian. *J. Paleoceanography*, **17**, https://doi.org/10.1029/2001PA000646.

Winguth, A. M. E., and C. Winguth, 2012: Precession-driven monsoon variability at the Permian-Triassic boundary – Implications for anoxia and the mass

extinction, *Global and Planetary Change*, **105**, 160-170, https://doi.org/10.1016/j.gloplacha.2012.06.006.

Xu, C., A. J. Boucot, C. R. Scotese, and F. Junxuan, 2012: Pangaean aggregation and disaggregation with evidence from global climate belts. *J. Palaeogeography*, **1**, 5-13.

Ziegler, A. M., J. M. Parrish, Y. Jiping, E. D. Gyllenhaal, D. B. Rowley, J. D. Parrish, N. Shangyou, A. Bekker, and M. L. Hulver, 1994: Early Mesozoic phytogeography and climate. *Palaeoclimates and their Modelling*, 89-97, https://doi.org/10.1007/978-94-011-1254-3_11.

Zobler, L., 1986: A wold soil file for global climate modeling. NASA Technical Memorandum 87802. NASA Goddard Institute for Space Studies, New York, New York, U.S.A.